CrystEngComm

Accepted Manuscript

ROYAL SOCIETY OF CHEMISTRY

www.rsc.org/crystengcomm

Computational Design of the Inorganic Nonlinear Optical Crystals Based on the Genetic Algorithm

Zhenxing Fang,[a] Jing Lin,[a] Rong Liu,[b] Ping Liu,[a] Yi Li,[*a] Xin Huang,[a] Kaining Ding,[a] Lixin Ning,[c] and Yongfan Zhang[*a,d]

[a] *College of Chemistry, Fuzhou University, Fuzhou, Fujian, 350116, China*

[b] *College of Mathematics and Computer Science, Fuzhou University, Fuzhou, Fujian, 350116, China*

[c] *Department of Physics, Anhui Normal University, Wuhu, Anhui, 241000, China*

[d] *Key Laboratory of Optoelectronic Materials Chemistry and Physics, Chinese Academy of Sciences, Fuzhou, Fujian, 350002, China*

Abstract Based on the results of density functional theory calculations, a theoretical method to design the inorganic nonlinear optical (NLO) crystals for the second harmonic generation (SHG) is presented. In this method, a specialized genetic algorithm (GA) is developed to search the stable structures of the inorganic crystal with known compositions, and then for the noncentrosymmetric stable structures, the second order nonlinear optical properties can be studied by calculating the corresponding SHG coefficients. Unlike the normal GA techniques, the main feature of the present method is that the coordination fashions of the building units are introduced to construct structures of individuals during the GA procedure, which can obviously improve the efficiency and success rate of obtaining the stable structure of inorganic crystals. As typical examples, two ternary compounds, $AgGaS_2$ and $LiAsSe_2$ crystals are considered, and besides the structure observed experimentally, the geometries and optical performances of other metastable (or more stable) phases have been explored. Our results clearly demonstrate that the present method can provide a feasible way to design and optimize new inorganic NLO crystals.

Key words: Second harmonic generation; genetic algorithm; density functional theory

[*] To whom correspondence should be addressed. E-mail: liy99@fzu.edu.cn; zhangyf@fzu.edu.cn

1. Introduction

The investigation of new second-order nonlinear optical (NLO) materials has attracted a considerable attention due to their important applications in optoelectronic technologies, such as optical parametric oscillator (OPO), difference frequency generation (DFG), laser frequency conversion, and signal communication.[1,2] Significant efforts have been made to develop of new NLO crystals, and in the past few years many new inorganic NLO crystals have been synthesized, including some metal chalcogenides(e.g., $APSe_6$ (A = K, Rb),[3,4] $AAsQ_2$ (A = Li, Na; Q = S, Se),[5,6] $AZrPQ_6$[7,8] and $A_4GeP_4Q_{12}$ (A = K, Rb, Cs; Q = S, Se),[9] Ln_4GaSbS_9 (Ln = Pr, Nd, Sm, Gd-Ho),[10] and Ln_3GaS_6 (Ln = Dy, Y)[11]), halides (e.g., $Rb_2CdBr_2I_2$,[12] $Cs_2HgI_2Cl_2$,[13] Hg_2Br_3I,[14] and HgBrCl[15]), and borates (e.g., $NaSr_3Be_3B_3O_9F_4$,[16] $Na_2Be_4B_4O_{11}$ and $LiNa_5Be_{12}B_{12}O_{33}$,[17] $Ba_4B_{11}O_{20}F$,[18] $Cd_5B_3O_9F$,[19] and $K_3B_6O_{10}Br$[20]). A NLO crystal with excellent performance requires several conditions to be satisfied, including high coefficient of second-order harmonic generation (SHG), wide transparent region, good phase matchability, a moderate laser damage threshold, and the availability of corresponding large-size crystal. However, many NLO crystals currently used have drawbacks in one or more respects, which causes difficulties in their applications. Therefore, the development of better NLO materials is still a subject with great challenge and worth deeply studying.

It is well known that only a noncentrosymmetric structure may possess second-order NLO effects, and correspondingly, major efforts have been paid to the construction of the noncentrosymmetric structures. On the basis of extensive experimental results, it is found that a common strategy to obtain noncentrosymmetric compounds is to incorporate asymmetric building blocks into the crystal structure.[21] These include second-order Jahn-Teller distorted d^0 early

transition-metal cations[22] (e.g., V^{5+} in $K_3V_5O_{14}$,[23] Mo^{6+} in $LaBMoO_6$[24] and $Na_2Te_3Mo_3O_{16}$,[25] Ta^{5+} in $Ag_2Ta_4O_{11}$,[26] and W^{6+} in $Na_2TeW_2O_9$[27]), and anionic groups with stereochemically active lone pairs (e.g., $(IO_3)^-$ in $BiO(IO_3)$[28] and AgI_3O_8,[29] $[AsS_3]^{3-}$ in $LiAsS_2$,[6] $[SbS_3]^{3-}$ in $Ba_{23}Ga_8Sb_2S_{38}$,[30] and $[TeS_3]^{2-}$ in Ag_2TeS_3[31]). However, we have to note that the introduction of the above asymmetric building units only enhance the possibility to yield conformation without inversion center, and the final structure still relies on whether they are packed in a noncentrosymmetric fashion.[21] Therefore, it is necessary to find effective ways to predict the mode of packing pattern of those asymmetric building blocks, as well as the associated NLO properties prior to the experiments.

In this paper, basing on the results of the first principles calculations, we propose a new method to design inorganic NLO material, in which the stable crystal structure of a compound with known composition is evaluated first by a specialized genetic algorithm (GA), combined with considering the structure of the building block, and then the corresponding optical properties are calculated theoretically by the length-gauge formalism. Using this method, the crystal structures and SHG effects of two ternary compounds, $AgGaS_2$ and $LiAsSe_2$ are determined and the results are compared with the experimental observations.

2. Method

2.1 The Overall Scheme of the Method

The flowchart of the method to design the NLO crystal is sketched in Figure 1. In the first step, the composition and stoichiometry of the compound are provided. As mentioned above, one or more asymmetric blocks with known configurations are introduced to make the formation of noncentrosymmetric structure more likely, and the additional cations or anions are further chosen to keep charge neutrality of the whole system. In the second step, a float encoding GA procedure is

carried out to search the stable crystal structure of the designed compound (see next section), followed by the identification of the space group to check whether the crystal structure contains an inversion center. If so, it needs to change the composition or stoichiometry of the compound and predict the structure again; otherwise in the next step the band gap and the momentum matrix elements will be calculated. Finally, by calculating the linear optical response properties and SHG coefficients, the optical performances of the designed material can be determined.

2.2 Prediction of the Stable Crystal Structure

There are some methods to solve the problem of the crystal structure prediction, such as simple random sampling, simulated annealing, and basin hopping, etc.[32] In here, a specialized GA approach is employed to find the low-lying structures on the potential energy surfaces of inorganic crystals, and the detailed procedure is also schematically illustrated in Figure 1. It must be mentioned that the present algorithm differs from the currently well-known USPEX (Universal Structure Prediction: Evolutionary Xtallography) method developed by Oganov group.[33,34] The main feature of our method is that the structural character of the building blocks is taken into account during GA procedure, and we will see that this treatment can improve the efficiency and success rate of structure predictions for the inorganic materials. The process includes the following steps (Figure 1):

(1) The first stage of GA procedure is to create the structures of the initial population $P(t)$ (t = 1). In this step, the population size (N) is assigned. In normal GA techniques (also including USPEX), the structures of the initial population is constructed randomly under some constraints (e.g. the smallest distances between two atoms). However, a different method that the atomic positions of cations and anions are treated separately is employed in here, and in Figure 2 the $AgGaS_2$ crystal is

used as an example to illustrate the detailed process. We first create the positions of all cations randomly, and then the positions of anions are determined according to the coordination fashions of the $[GaS_4]^{5-}$ building blocks. In the latter step, the configuration of $[GaS_4]^{5-}$ unit (e.g. a perfect tetrahedron) can be defined by providing the Cartesian coordinates of four S anions (the position of Ga cation is set at the origin). Using this $[GaS_4]^{5-}$ unit as a prototype and after rotating it randomly around the *z* and *x* axes, we can construct all $[GaS_4]^{5-}$ tetrahedra in the cell that their orientations are arranged randomly (see tetrahedron.m code in the Supporting Information). Finally, to maintain the stoichiometry of the system and to avoid some anions too close together, those excessive anions are removed by examining the distance between two nearest-neighbor anions.

(2) The first principles code is employed to optimize the structure of each individual in current population, and the corresponding total energy and space group are obtained (see cal_energy_list.m code in the Supporting Information).

(3) Check whether the termination condition is satisfied. The common criterion includes a limit on the maximum generation number (t_{max}) or the number of successive generations that the best individual remains unchanged.

(4) Rank the individual in the population according to the total energy, and some individuals with high energy are eliminated with a given probability (P_e) and the new breading pool is created.

(5) For the rest individuals, the genetic operators are applied to build the new structures. In here three operators, heredity, swap and mutation are considered. First, the remaining individuals are paired with the lowest energy individual of the current generation, and crossover operation is employed to create new points in the search space according to a given probability (P_c). It is noted that only cations are involved in heredity, while the positions of anions are determined by the

similar method as mentioned in the step (1). Then for those individuals that are not involved in heredity, two types of atoms are selected randomly, and their positions are exchanged. Finally, the mutation operation is performed for above new structures to introduce a perturbation for a selected structural parameter at a given probability (P_m).

(6) Similar to the step (1), regenerate structures of those individuals eliminated in step (4), and the population size remains unchanged.

(7) To keep the best individual of current generation to the next generation, it needs to delete an individual at random, and then replace it with the individual with the lowest energy. Now all the individuals of the new generation, *P(t+1)* are created.

(8) Go back to step (2) until the termination condition is met.

In the present work, the Vienna *ab initio* simulation package (VASP)[35,36,37] based on density functional theory (DFT) was employed to relax the geometry (including the cell parameters and atomic positions) of each individual. During the calculations, the projector-augmented wave (PAW) pseudopotentials and a generalized gradient approximation (GGA) in the Perdew-Burke-Ernzerhof (PBE) flavor for exchange and correlation effects were adopted. The convergence thresholds of the energy change and the maximum force for the geometry optimizations were set to 10^{-5} eV and 0.01 eV/Å, respectively. In addition, the spglib package was used to identify the space group of the optimized crystal.[38]

2.3 Prediction of the Optical Properties for the NLO Crystal

When the predicted crystal exhibits a noncentrosymmetric structure, the associated optical properties will be evaluated in the next step. The linear optical response is directly related to the complex dielectric function $\varepsilon(\omega) = \varepsilon_1(\omega) + i\varepsilon_2(\omega)$, and the imaginary part of the dielectric

function, $\varepsilon_2(\omega)$ is given by following equation,[39]

$$\varepsilon_2^{ab}(\omega) = \frac{4\pi^2}{V}\sum_{nm,k} f_{nm}\frac{r_{nm}^a r_{mn}^b}{\omega_{nm}-\omega} \quad (1)$$

where superscripts, *a* and *b* indicate Cartesians components; *n* and *m* represent the energy bands; $f_{nm} = f_n - f_m$ is the difference of the Fermi distribution functions; $\omega_{mn} = \omega_m - \omega_n$ is the frequency difference for the bands *m* and *n*; *V* is the unit cell volume. The r_{nm}^a is the matrix element of the position operator that is defined as,

$$r_{nm}^a = \frac{-ip_{nm}^a}{\omega_{nm}} \quad (2)$$

where p_{nm} is the momentum matrix element. The real part of the dielectric function is obtained from $\varepsilon_2(\omega)$ by a Kramer-Kronig transformation. By using the dielectric function, all other linear optical properties, including refractive index, birefringence, reflectivity, and adsorption spectrum can be derived.

The second-order nonlinear susceptibility $\chi^{abc}(-2\omega,\omega,\omega)$ is calculated at the independent-particle level. The corresponding formalism was firstly introduced by Aversa and Sipe,[40] and later was rearranged by Rashkeev *et al*.[41] to explicitly exhibit the Kleinman symmetry,[42] in which the susceptibility for the SHG of an insulator or a semiconductor can be divided into the contribution of the interband transitions $\chi_e^{abc}(-2\omega,\omega,\omega)$ and the contribution of the mixed interband and intraband transitions $\chi_i^{abc}(-2\omega,\omega,\omega)$, namely,

$$\chi^{abc}(-2\omega,\omega,\omega) = \chi_e^{abc}(-2\omega,\omega,\omega) + \chi_i^{abc}(-2\omega,\omega,\omega) \quad (3)$$

At zero frequency limit, above two contributions are given by following equations,[41]

$$\chi_e^{abc} = \frac{1}{V}\sum_{nml,k}\frac{r_{nm}^a\{r_{ml}^b r_{ln}^c\}}{\omega_{nm}\omega_{ml}\omega_{ln}}[\omega_n f_{ml} + \omega_m f_{ln} + \omega_l f_{nm}] \quad (4)$$

$$\chi_i^{abc} = \frac{i}{4V}\sum_{nm,k}\frac{f_{nm}}{\omega_{mn}^2}[r_{nm}^a(r_{mn;c}^b + r_{mn;b}^c) + r_{nm}^b(r_{mn;c}^a + r_{mn;a}^c) + r_{nm}^c(r_{mn;b}^a + r_{mn;a}^b)] \quad (5)$$

where $r_{mn;a}^b$ is the generalized derivative of the position operator,

$$r_{mn;a}^b = \frac{r_{nm}^a\Delta_{mn}^b + r_{nm}^b\Delta_{mn}^a}{\omega_{nm}} + \frac{i}{\omega_{nm}}\sum_l(\omega_{lm}r_{nl}^a r_{lm}^b - \omega_{nl}r_{nl}^b r_{lm}^a) \quad (6)$$

where $\Delta_{mn}^a = (p_{nn}^a - p_{mm}^a)/m$ is the difference between the electronic velocities at the energy bands *n* and *m*. While for the frequency-dependent SHG susceptibility (namely $\omega > 0$), [41]

$$\chi_e^{abc}(-2\omega,\omega,\omega) = \frac{1}{V}\sum_{nml,k}\frac{r_{nm}^a\{r_{ml}^b r_{\ln}^c\}}{(\omega_{\ln} - \omega_{ml})}[\frac{2f_{nm}}{\omega_{mn} - 2\omega} + \frac{f_{\ln}}{\omega_{\ln} - \omega} + \frac{f_{ml}}{\omega_{ml} - \omega}] \quad (7)$$

$$\chi_i^{abc}(-2\omega,\omega,\omega) = \frac{i}{2V}\sum_{nm,k}f_{nm}[\frac{2}{\omega_{mn}(\omega_{mn} - 2\omega)}r_{nm}^a(r_{nm;c}^b + r_{mn;b}^c) + \frac{1}{\omega_{mn}(\omega_{mn} - \omega)}(r_{nm;c}^a r_{mn}^b + r_{nm;b}^a r_{mn}^c)$$

$$+\frac{1}{\omega_{mn}^2}(\frac{1}{\omega_{mn} - \omega} - \frac{4}{\omega_{mn} - 2\omega})r_{nm}^a(r_{mn}^b\Delta_{mn}^c + r_{mn}^c\Delta_{mn}^b) - \frac{1}{2\omega_{mn}(\omega_{mn} - \omega)}(r_{nm;a}^b r_{mn}^c + r_{nm;a}^c r_{mn}^b)] \quad (8)$$

According to Eqs.(3)-(8), we have written corresponding code to calculate the static and dynamic SHG coefficients from the results obtained by VASP program. Since a very dense sampling of k space and many energy bands are required in the second-order nonlinear susceptibility calculations, it is normally time-consuming to predict the SHG coefficients. Based on Message Passing Interface (MPI), the parallel implementation of the above method for computing SHG coefficients has been realized in our code by distributing data over k-points on each compute core.[43] Additionally, due to the band gap of the semiconductor or insulator is usually underestimated by the pure DFT method, the correction to the band structure is necessary. In here, the "scissors" approximation proposed by Levine and Allan was employed,[44] which consists of a shift of all the conduction bands by a gap correction. In the following sections the *d*-tensor defined as $d_{ij} = \chi^{abc}/2$ was used to represent second-order nonlinear optical susceptibility, in which Voigt notation indices were introduced to simplify second rank tensors.

3. Application Examples

For the purposes of testing, two already reported ternary inorganic crystals, $AgGaS_2$ and $LiAsSe_2$ are selected as typical examples to verify the reliability and stability of above method.

3.1 $AgGaS_2$

Silver thiogallate crystal ($AgGaS_2$) is the most common and representative NLO crystal in the infrared region (IR) and has been widely used for DFG and OPO. It is well known that $AgGaS_2$ crystallizes in the noncentrosymmetric $I\bar{4}2d$ space group, namely the so-called chalcopyrite structure.[45] Using the above algorithm, we first predict the low-lying structures on the potential energy surface of $AgGaS_2$, and the calculations by the universal USPEX method (version 9.3.9)[33,34] are also performed for comparison. In here, the small and large $AgGaS_2$ cells are taken into account, which contain 8 and 16 atoms, respectively. In order to examine the performance, each algorithm is run four times, and the population sizes and the maximum number of generations are 10 and 5 for the small cell, 30 and 10 for the large cell, respectively. The parameters adopted in our GA procedure are P_e = 0.2, P_c = 0.6, and P_m = 0.1, while the default settings are used for the USPEX method. The structure of each individual was optimized by employing PBE functional, and the kinetic energy cutoff for the plane-wave expansion was set to 350 eV. The Brillouin zone was sampled using the Monkhorst-Pack approximation and a gird of k-points separated by 0.08 $Å^{-1}$.

Before discussing the best individual, it is necessary to evaluate our method to build the structures of the initial population. Using the large $AgGaS_2$ cell as an example, the average energies of the initial population predicted by USPEX are -59.0342, -59.0157, -58.4865, and -58.3873 eV, respectively. However, the lower average energies, -61.2589, -61.1905, -61.0434, and -60.7819 eV are achieved by applying our method. Therefore, compared with the normal method that the

structures of the first population are created in a completely randomized manner, the present way can produce more reasonable structures after considering the configurations of the $[GaS_4]^{5-}$ building blocks. Some information of the best individual with the lowest energy obtained by two approaches, including which generation it is observed, the source, and corresponding space group, is listed in Table 1. For the small $AgGaS_2$ cell, the experimental structure ($I\bar{4}2d$ space group) is obtained successfully every time by the present GA; while at one test running the USPEX fails to yield the experimental structure, and a metastable phase that adopts the $Pmc2_1$ space group is predicted. Additionally, it is worthy noting that in most cases (three out of four tests), the experimental structure is quickly located at the first generation. When a large $AgGaS_2$ cell is employed, although more generations are required, the chalcopyrite phase is still predicted to be the most stable structure every time by the present method. As a comparison, by using the USPEX, the experimental structure is achieved only in one out of four tests, and in most cases other metastable structures are obtained within ten generations. The above results show that present specialized GA method can improve the efficiency and success rate of the structure predictions for the inorganic materials. This is mainly because our method has two advantages over normal GA technique: (a) it is more reasonable to construct the initial structure of each individual by considering the coordination fashion of the building unit. In other words, we can arrange more individuals around the local minima of the potential energy landscape, and consequently, for a fixed population size, the possibility to find the stable or metastable states is improved; (b) as a result of that only cations are involved in the crossover operation, the actual number of atom is reduced during the heredity process, which is advantageous for a system containing more atoms. For instance, although there are 16 atoms in the large $AgGaS_2$ cell, only eight cations (i.e. 4 Ag^+, and 4 Ga^{3+} ions) are taken part

in the crossover operation.

By comparing the total energy of each individual, three low-lying structures of $AgGaS_2$ crystals shown in Figure 3 are found within 0.1 eV/formula unit, and the corresponding space group, lattice parameters, fractional atomic positions, the lengths of Ga-S bonds, and relative energy are summarized in Table 2. It is interesting that all three structures are noncentrosymmetric, implying that the silver thiogallate tends to crystallize in polar phases at normal pressure. Although in these structures the $[GaS_4]^{5-}$ tetrahedra are connected to each other via corner-sharing, the detailed configurations and alignments of the $[GaS_4]^{5-}$ tetrahedra are different. For the most stable $I\bar{4}2d$ phase, all $[GaS_4]^{5-}$ tetrahedra have the same orientation and the length of four Ga-S bonds are identical. While in the $Pna2_1$ structure (Figure 3b) that is only 11.87 meV/formula higher in energy, the $[GaS_4]^{5-}$ tetrahedra are distorted slightly and show two different orientations along the *c* axis. As far as the third low-lying structure (Figure 3c) is concerned, it features a layered packing of the $[GaS_4]^{5-}$ tetrahedra separated by Ag^+ cations, whereas in the $I\bar{4}2d$ and $Pna2_1$ phases the $[GaS_4]^{5-}$ tetrahedral units are condensed each other via corner-sharing to form a three-dimensional framework.

After obtaining the stable structure with noncentrosymmetric arrangement, we then can explore the optical properties of $AgGaS_2$ crystal with $I\bar{4}2d$ phase. In this step, a very dense k-point mesh of (21 × 21 × 21) (resulting in 4631 k points in the first Brillouin zone) was employed to guarantee the convergences of the results of the linear and nonlinear optical responses, and the energy cutoff for those empty energy bands involved in the calculations was taken to be at least 30 eV above the valence-band maximum. Moreover, to overcome the well-known band gap problem of DFT method, a scissor operator of 1.73 eV was applied to reproduce the experimental band gap 2.64 eV.[46]

For the linear optical response, the $AgGaS_2$ with tetragonal phase belongs to uniaxial crystal, and there are two dielectric tensor components, corresponding to electric field perpendicular and parallel to the *c*-axis (namely $\varepsilon^{\perp}(\omega)$ and $\varepsilon^{//}(\omega)$, respectively). The predicted complex dielectric functions for the most stable $I\bar{4}2d$ structure are displayed in Figures 4a and 4b. From the dielectric function, the refractive indices, $n^{\perp}(\omega)$ and $n^{//}(\omega)$ can be obtained, and then the birefringence $\Delta n(\omega)$ can be determined from the difference between two refraction indices, which are also shown in Figure 4c and 4d, respectively. Additionally, the corresponding static dielectric constants ($\varepsilon(0)$), refractive indices ($n(0)$), and birefringence ($\Delta n(0)$) are listed in Table 3, and the results of other theoretical works and some available experimental values of $AgGaS_2$ with $I\bar{4}2d$ structure are also shown for comparison.[47,48,49,50,51] The calculated refractive indices in the present work agree well with the values of experimental measurements, while the results obtained in other theoretical studies are somewhat overestimated. From Figure 4d, it can be seen that the negative birefringence is predicted when the wavelength (λ) is larger than 0.490 μm (i.e. 2.53 eV). This critical wavelength is also in good agreement with the experimental observation that $AgGaS_2$ is a negative uniaxial crystal at $\lambda > 0.497$ μm.[49] As for the SHG response of $AgGaS_2$ in chalcopyrite phase, there are only two independent components of the SHG tensor, namely, d_{14} and d_{36}, respectively. In the static limit, these two components are equal according to the Kleinman symmetry, and our calculated result of 17.47 pm/V is very close to the experimental value of 18 ± 2.7 pm/V (at 10.63 μm).[51] Therefore, the method mentioned in Section 2.3 is suitable for predicting the optical properties of semiconductors. We also calculate the frequency-dependent SHG coefficient of $AgGaS_2$ by using Eqs. (7) and (8), and the result is displayed in Figure 5a. At the beginning when the energy is less than 1.0 eV, the d_{36} coefficient increases slowly. With further

increasing of the energy, the SHG response rapidly increases, and in the IR region it exhibits a maximum value of 51.17 pm/V at about 1.38 eV.

To see how the structure of the $[GaS_4]^{5-}$ building units affects the optical performances of $AgGaS_2$ crystal, we also investigate the optical properties of $AgGaS_2$ crystallized in the *Pna2₁* and *Pmc2₁* structures. In the case of *Pna2₁* phase, a (15 × 12 × 15) k-point mesh that yields 1351 k points in the first Brillouin zone was employed. For this metastable structure, a direct band gap of 1.06 eV is obtained, about 0.15 eV larger than the gap of $I\bar{4}2d$ structure. The *Pna2₁* phase belongs to biaxial crystal, and there are three dielectric tensor components, and if the same scissor energy (1.73 eV) was used, the calculated static dielectric constants are $\varepsilon^{xx}(0) = 6.121$, $\varepsilon^{yy}(0) = 6.179$, $\varepsilon^{zz}(0) = 6.254$, respectively. Correspondingly, three static refractive indices are $n^{xx}(0) = 2.474$, $n^{yy}(0) = 2.486$, $n^{zz}(0) = 2.501$, respectively, resulting in $\Delta n(0) = 0.027$. The small magnitude of birefringence implies the poor performance of the phase matchability for the *Pna2₁* phase. The frequency-dependent SHG coefficient for the highest tensor of *Pna2₁* phase (d_{33}) is shown in Figure 5a, and compared with the $I\bar{4}2d$ structure, the SHG response becomes weakened at the near IR region. For another metastable *Pmc2₁* structure that is composed of the layered packing of the $[GaS_4]^{5-}$ blocks, a small direct band gap of 0.69 eV is predicted, and when the same scissor energy is employed, the magnitude of $\Delta n(0)$ is about 0.089. This increase of the birefringence is consistent with the fact that the layered arrangement of the $[GaS_4]^{5-}$ units favors a strong optical anisotropy. Additionally, according to the frequency-dependent SHG coefficient displayed in Figure 5a, it seems that the SHG response is enhanced at the far IR region. Therefore, the configuration and the packing mode of the $[GaS_4]^{5-}$ blocks have obvious effects on the optical properties of $AgGaS_2$, including the transparency range, the phase matchability and the strength of the SHG response.

3.2 $LiAsSe_2$

It is well known that the chalcogenide compounds usually have a small band gap and high second-order nonlinearity, so they are good candidates for NLO materials in IR region. In recent years, many promising chalcogenide compounds have been discovered with novel compositions and crystal structures, which can be used to produce the next generation of NLO materials in the IR region (e.g., see a recent review by Chung and Kanatzidis[21]). Among them, a new class of polar semiconductors, $AAsSe_2$ (A = Li, Na) have been synthesized.[5] The main structural feature of these chalcogenides is the infinite single chains of $^1_\infty[AsSe_2^-]$ derived from corner-sharing pyramidal asymmetric $[AsSe_3]^{3-}$ units. For $NaAsSe_2$, a very strong SHG response in the wavelength range of 600 ~ 950 nm has been observed experimentally, and several theoretical studies have also confirmed the experimental results that $NaAsSe_2$ has the large static SHG coefficient more than 300 pm/V.[5,52,53] In the present work, we will focus on structure and optical properties of another alkali-metal chalcogenide, $LiAsSe_2$. For the primitive cell of $LiAsSe_2$, there are two Li, two As, and four Se atoms. The parameters used in the GA procedure are t_{max} = 50, N = 12, P_e = 0.2, P_c = 0.6, and P_m = 0.1. During the DFT/PBE calculations, the kinetic energy cutoff for the plane-wave expansion was set to 264.4 eV, and the k-point separation was about 0.08 $Å^{-1}$.

With respect to $AgGaS_2$ above mentioned, the crystal structure of $LiAsSe_2$ is somewhat complicated. By examining the geometries of those individuals with low energies, as shown in Figure 6, three stable phases of $LiAsSe_2$ are predicted, which are crystallized in the noncentrosymmetric space groups of *Pm* (No. 6), *Cc* (No. 9), and $Pmc2_1$ (No. 26), respectively. The corresponding structural parameters and the relative energy per $LiAsSe_2$ formula are listed in Table 4. In here, the relative energies are calculated at dense k-point meshes with a separation of about

0.01 $Å^{-1}$. For the fourth structure, it belongs to the space group $P2_1$ with a quasi-cubic unit cell (see Table S1 in the Supporting Information), and due to this structure is higher in energy (about 30 meV per formula with respect to the *Pm* phase), the corresponding results are not shown. Among them, the structure in the *Cc* space group has been experimentally reported.[5] Furthermore, to check the dynamic stability of the predicted *Pm* and $Pmc2_1$ structures, their phonon dispersion curves are also calculated, and no imaginary frequency is observed (see Figure S1 in the Supporting Information), implying that both phases are dynamically stable.

As shown in Figure 6, the $[AsSe_3]^{3-}$ pyramid provides the basic building blocks of all three stable structures, and *via* corner bridging the one-dimensional $^1_\infty[AsSe_2^-]$ chains are formed. In each $[AsSe_3]^{3-}$ trigonal pyramid, it has two different Se atoms, namely the terminal and bridging Se atoms, respectively. Although according to the lengths of two kinds of As-Se bonds (Table 4) the configurations of the $AsSe_3$ building units are quite analogous, various conformations of the $^1_\infty[AsSe_2^-]$ chains are observed in different crystal structure. In the *Pm* and $Pmc2_1$ phases, the orientations of the $[AsSe_3]^{3-}$ units of the single chain are the same, and as a result the pyramids are arranged in an ordered fashion. However, it must be mentioned that, the relative orientations between two $^1_\infty[AsSe_2^-]$ chains in the unit cell of $Pmc2_1$ are different (see Figure 6c). Unlike the *Pm* and $Pmc2_1$ phases, there are two orientations of the $[AsSe_3]^{3-}$ blocks observed within a single chain of the *Cc* structure, and now the pyramids show a zigzag alignment. Actually, for the fourth structure with the space group $P2_1$, it adopts another different zigzag conformation of $^1_\infty[AsSe_2^-]$ chains (see Table S1 in the Supporting Information). From the relative energies of three structures shown in Table 4, it is interesting that the energy difference among them is quite small (< 4.0 meV per formula). Thus we can expect that above three phases would coexist from a thermodynamical

point of view. This result is consistent with the experimental findings that the $^{1}_{\infty}[AsSe_2^-]$ single chain exhibits remarkable conformational flexibility and is readily influenced by the synthetic conditions as well as the alkali-metal species.[5]

Considering above three structures are noncentrosymmetric and the packing of asymmetric $[AsSe_3]^{3-}$ units are different, $LiAsSe_2$ provides a rare example to explore how the conformational change of the building units affects the optical properties of the material. In the optical response calculations, the sizes of k-point mesh of the *Pm*, *Cc* and *Pmc2₁* phases were set to (25 × 26 × 17), (20 × 20 × 20), and (25 × 25 × 9), respectively, corresponding to 5526, 4004, and 2813 k points in the first Brillouin zone. The calculated minimum band gaps of three compounds at PBE level are listed in Table 5, and by comparing the experimentally measured band gap (1.11 eV) of *Cc* structure,[5] a scissor operator of 0.44 eV was employed in the optical calculations of three systems. For the linear optical response, the dielectric tensors of these biaxial crystals are calculated along the principal optical axes, and the results of $LiAsSe_2$ with *Pm* structure are presented in Figure 7a and 7b (see Figures S2 and S3 in the Supporting Information for the *Cc* and *Pmc2₁* phases). The frequency-dependent dielectric function of *Pm* structure shows strong anisotropy in the IR region, resulting in the significant difference among three static dielectric constants that are $\varepsilon^{xx}(0) = 8.791$, $\varepsilon^{yy}(0) = 16.753$, and $\varepsilon^{zz}(0) = 23.560$, respectively (Table 5). The sharp peaks of the imaginary part of ε^{zz} observed in the IR region can be mainly assigned to the transitions from the Se 4p to As 4p states. As a consequence of the anisotropy of the dielectric functions, the curves of refractive indices (Figure 7c) also exhibit strong anisotropy. In the IR region the sequence of three refractive indices is $n^{xx} < n^{yy} < n^{zz}$, and the values of $n^{xx}(0)$, $n^{yy}(0)$, and $n^{zz}(0)$ are 2.965, 4.093, and 4.854, respectively. Since n^{zz} is significantly larger than n^{xx}, the high values of birefringence (Δn) of the

Pm structure can be expected. At the static limit a value of 1.889 is calculated for $\Delta n(0)$ (Table 5), and as displayed in Figure 7d the birefringence is larger than 1.8 in the IR region, suggesting $LiAsSe_2$ crystal in the *Pm* space group is phase-matchable in this region. However, unfortunately, above large birefringence will require a very narrow acceptance angle of the incident light, which is particularly unfavorable for practical application in the NLO field. Similar results for the linear optical response are obtained for the *Cc* and $Pmc2_1$ phases, and especially they also appear high birefringence in the IR region (see Figure 7d). It is obvious that the strong anisotropic feature of $LiAsSe_2$ crystal with different phases is directly related to the one-dimensional structure of $^1_\infty[AsSe_2^-]$ chains, and the degree of anisotropy presents a strong correlation with the chain conformations. The strongest anisotropy is observed for the *Pm* and $Pmc2_1$ structures with the same orientation of each $[AsSe_3]^{3-}$ pyramid within a chain, while the *Cc* structure shows a relatively weak anisotropy due to the zigzag packing pattern of the $[AsSe_3]^{3-}$ pyramids (Figure 6). As shown in Figure 7d, the maximum birefringence of the *Pm* and $Pmc2_1$ structures is about 3.9, and it is ~1.6 times larger than that of the *Cc* structure.

Now, let us discuss the SHG responses of three $LiAsSe_2$ crystals. Based on the space groups and the Kleinman symmetry, at static limit there are 6, 6, and 3 nonvanishing independent SHG coefficients for $LiAsSe_2$ crystallized in the *Pm*, *Cc* and $Pmc2_1$ space groups, respectively. As listed in Table 5, the static SHG coefficients with the highest magnitudes of three compounds are d_{34}(= d_{23}) for *Pm*, d_{33} for *Cc*, and d_{11} for $Pmc2_1$ structures, with the values of 1379.57, 737.72, and 141.36 pm/V, respectively. The frequency-dependent variations of these SHG tensors are plotted in Figure 5b. In the mid-IR and far-IR regions, the magnitudes of above SHG coefficients tend to follow a sequence of *Pm* > *Cc* > $Pmc2_1$, and the position of the peak maximum is blue-shifted in the same

order. It is worth emphasizing that, besides the relatively small value of the band gap, the extremely strong nonlinear SHG response observed for the *Pm* structure is also associated with its special arrangement of the $[AsSe_3]^{3-}$ pyramids. Since the intensity of the second order susceptibility for a polar material is directly related to the net dipole moment of the unit cell,[54] it is necessary to compare the alignment of dipole moment of asymmetric $[AsSe_3]^{3-}$ unit in three structures (the dipole moment of the spherical Li^{1+} cation is zero). In here, a simple bond-valence approach[55] is used to estimate the direction and magnitude of the dipole moment of the $[AsSe_3]^{3-}$ group, and for simplicity the contribution of As^{3+} lone-pair electrons is not considered. Due to the resemblance in the configuration, the dipole moment of the individual $[AsSe_3]^{3-}$ group of three phases is similar (in the range from 26.2 to 27.2 Debye). The calculated microscopic dipole moments of different $LiAsSe_2$ crystals are listed in Table 6, and the corresponding directions are represented by graphical arrows in Figure 8. It is noted that for the *Cc* and *Pmc2₁* structures, there are two $[AsSe_3]^{3-}$ groups in the primitive cell, which are belonged to the same and different $^{1}_{\infty}[AsSe_2^{-}]$ chains (Figure 6), respectively. For the *Pm* structure, the dipole moments of the $[AsSe_3]^{3-}$ groups align in the same direction (Figure 8a), to give a polar structure without cancellation of the individual moments, and thus the maximum magnitude of the total microscopic dipole (0.295 Debye per volume) is achieved. However, in the *Cc* structure (Figure 8b), the different orientation of the adjacent $[AsSe_3]^{3-}$ groups within a chain leads to a partially cancelling of the neighboring dipole moments. As shown in Table 6, the component of dipole moment along the *y*-axis is entirely cancelled each other, resulting a microscopic dipole moment with moderate magnitude (0.224 Debye per volume). Another different kind of dipole-dipole interaction is observed for the *Pmc2₁* structure (Figure 8c), in which the cancellation of the neighboring dipole moments is interchain along the *y*-axis. In this case, a

relatively small magnitude of microscopic dipole moment (0.136 Debye per volume) is predicted. From the above results the dipole moments of three $LiAsSe_2$ crystals increase in the order of $Pmc2_1$ < *Cc* < *Pm*, and correspondingly the intensity of SHG response is enhanced following the same trend of polarizability. Therefore, it is evident that, the large SHG coefficient obtained for the *Pm* space group is mainly originated from the same alignment of all $[AsSe_3]^{3-}$ trigonal pyramids with no cancellation of the individual moments. Although, as pointed above, the strong anisotropy of this series of crystals causes the limitation in the NLO applications, the excellent birefringence property makes $LiAsSe_2$ crystals have potential applications in optical polarization component.

4. Conclusions

In this work, we propose a calculational method to design inorganic NLO crystals, which takes into account the stable crystal structure predictions by a specialized GA technique and the theoretical calculations of the static and frequency-dependent SHG coefficients. This new method has been validated by applying it to two typical systems, $AgGaS_2$ and $LiAsSe_2$ crystals. The experimental structure, linear and nonlinear optical properties of $AgGaS_2$ are well reproduced, while for $LiAsSe_2$, besides the experimental structure in the *Cc* phase, two other stable structures are predicted by our method, and especially the structure crystallized in the *Pm* space group shows remarkable birefringence feature and very strong SHG response in the IR region. The present results clearly demonstrate that our method can provide an effective way to find new inorganic NLO materials if the composition of the system and the coordination fashions of the building units are known beforehand. The further works to design more complicated inorganic NLO crystals are in progress.

Acknowledgements

This work was supported by National Natural Science Foundation of China (grant nos. 21373048, 21373034, 21233009, 11174005, 21171039, 21203027, and J1103303), the Open Foundation of Key Laboratory for High-Energy Laser Science of China Academy of Engineering Physics (2012HCF05), the Fund of Key Laboratory of Optoelectronic Materials Chemistry and Physics, Chinese Academy of Sciences (2008DP173016), and Natural Science Foundation of Fujian Province for Distinguished Young Investigator Grant (2013J06004).

Electronic supplementary information (ESI) available: Calculated phonon dispersion curves for the *Pm* and *Pmc2$_1$* phases of $LiAsSe_2$ crystal, the linear optical responses of $LiAsSe_2$ crystals crystallized in the *Cc* and *Pmc2$_1$* space groups, the lattice constants and fractional atomic positions of the $LiAsSe_2$ in the *P2$_1$* space group, and part of the source code used in the present work.

Figure Captions

Figure 1 Flow diagram of the method to design NLO crystal.

Figure 2 Three steps to construct a structure of the initial population of $AgGaS_2$ crystal: (a) The crystal cell and the positions of Ag and Ga cations are constructed randomly; (b) The $[GaS_4]^{5-}$ tetrahedral units are created for each Ga cation, in this step the Ga-S bond lengths and the S-Ga-S bond angles are defined by user while the orientations of the $[GaS_4]^{5-}$ units are arranged randomly; (c) Eight S atoms are removed by examining the distance between two nearest-neighbor S atoms. In here, we assume that there are four Ag, four Ga, and eight S atoms in the unit cell of $AgGaS_2$ crystal, and in the final structure shown in (c), four Ga atoms are 4-fold, 3-fold, 3-fold, and 2-fold coordinated, respectively. The Ag, Ga and S atoms are denoted by blue, brown and yellow spheres, respectively.

Figure 3 The structures of $AgGaS_2$ that crystallizes in the (a) $I\bar{4}2d$, (b) $Pna2_1$, and (c) $Pmc2_1$ space groups predicted by the GA method. The Ag, Ga and S atoms are denoted by gray, cyan and yellow spheres, respectively, and the $[GaS_4]^{5-}$ tetrahedra are denoted by gray polyhedrons. The unit cell is shown in dark lines.

Figure 4 The calculated complex dielectric functions of (a) $\varepsilon^{\perp}(\omega)$ and (b) $\varepsilon^{//}(\omega)$, (c) the refractive indices $n(\omega)$, and (d) the birefringence $\Delta n(\omega)$ of $AgGaS_2$ crystallized in the $I\bar{4}2d$ space group.

Figure 5 Calculated frequency-dependent SHG coefficients for (a) $AgGaS_2$ and (b) $LiAsSe_2$ crystallized in different space groups.

Figure 6 The structures of three stable $LiAsSe_2$ crystals that crystallize in the (a) *Pm*, (b) *Cc*, and (c) $Pmc2_1$ space groups predicted by the GA method. The Li, As and Se atoms are denoted by gray, cyan and yellow spheres, respectively, and the $[AsSe_3]^{3-}$ pyramid is denoted by gray polyhedrons. The unit cell is shown in dark lines.

Figure 7 The calculated (a) real part and (b) imaginary part of complex dielectric functions, (c) the refractive indices, and (d) the birefringence of $LiAsSe_2$ that crystallizes in the *Pm* space group.

Figure 8 Directions of the calculated microscopic dipole moments of the $[AsSe_3]^{3-}$ groups in $LiAsSe_2$ crystals crystallized in the (a) *Pm*, (b) *Cc*, and (c) $Pmc2_1$ space groups. The Li, As and Se atoms are denoted by gray, cyan and yellow spheres, respectively, and the $[AsSe_3]^{3-}$ pyramid is denoted by gray polyhedrons.

Figure 1

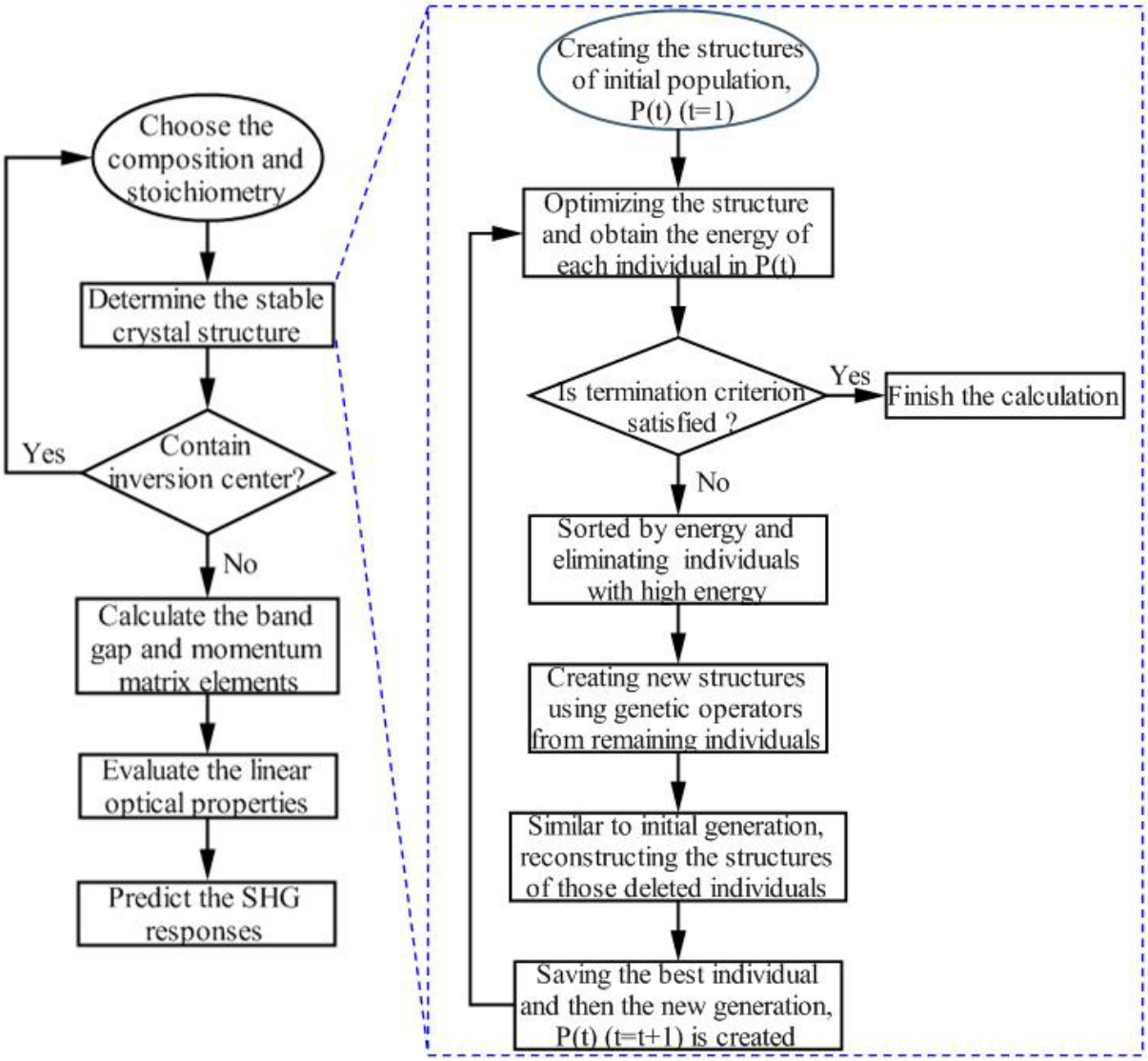

Figure 2

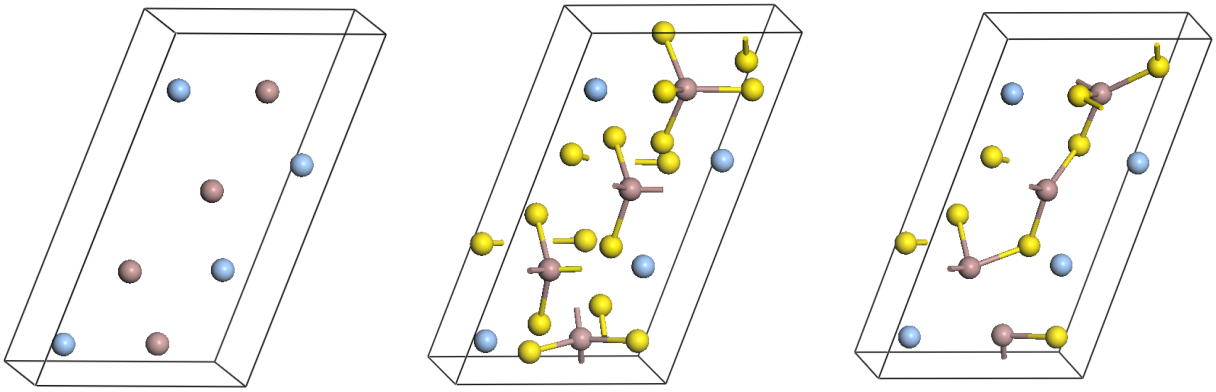

(a) (b) (c)

Figure 3

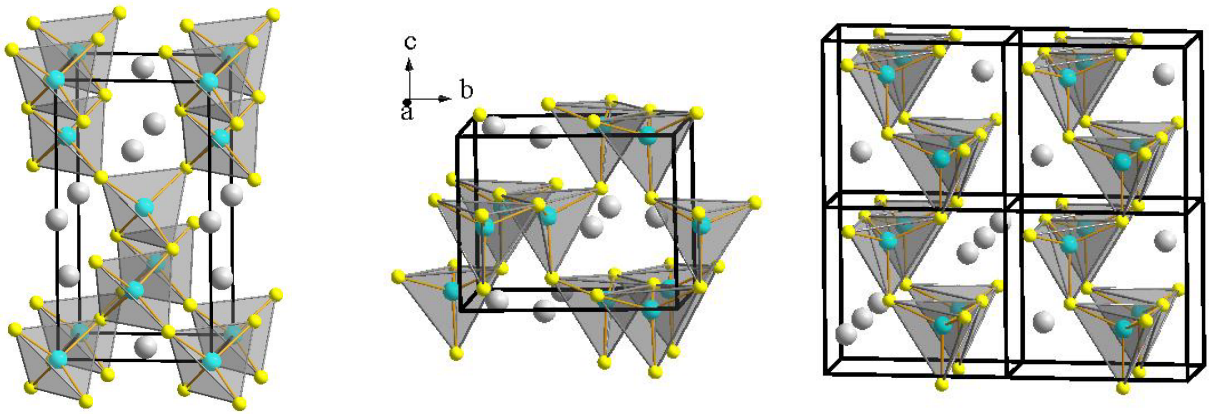

(a) (b) (c)

Figure 4

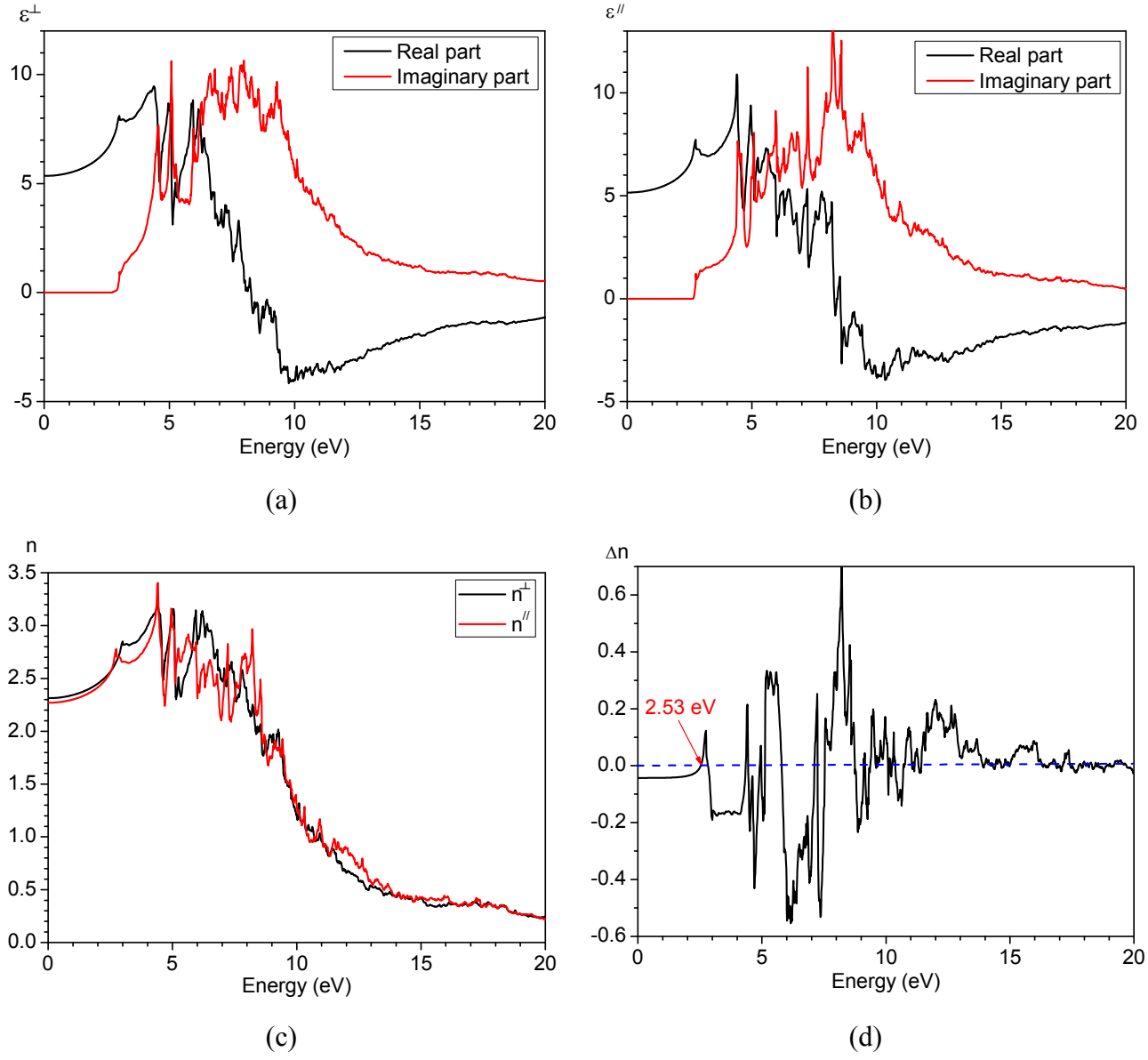

Figure 5

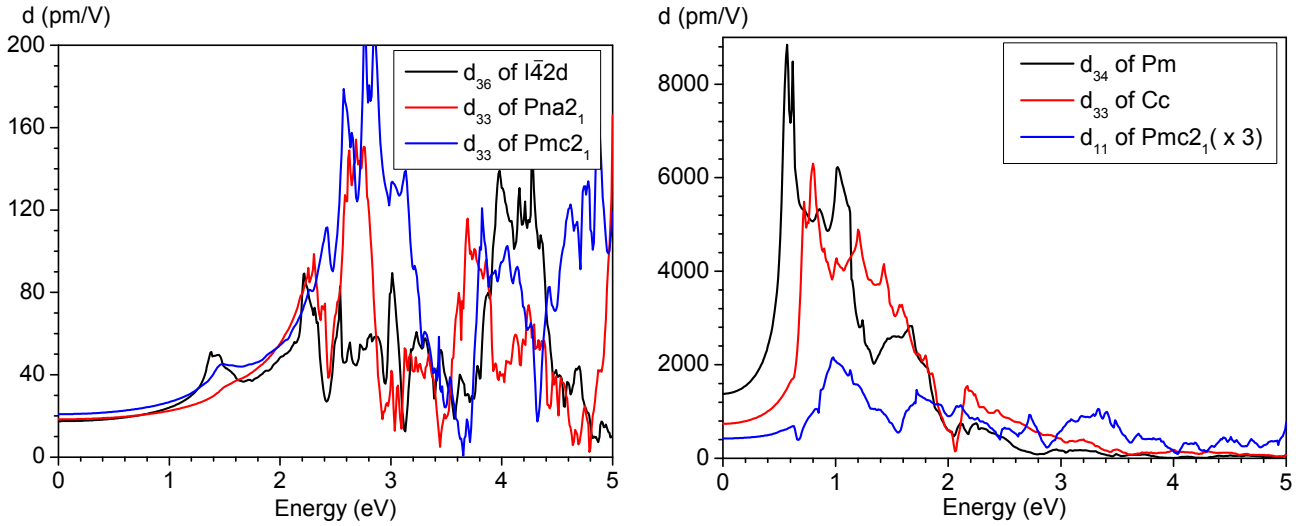

(a) (b)

Figure 6

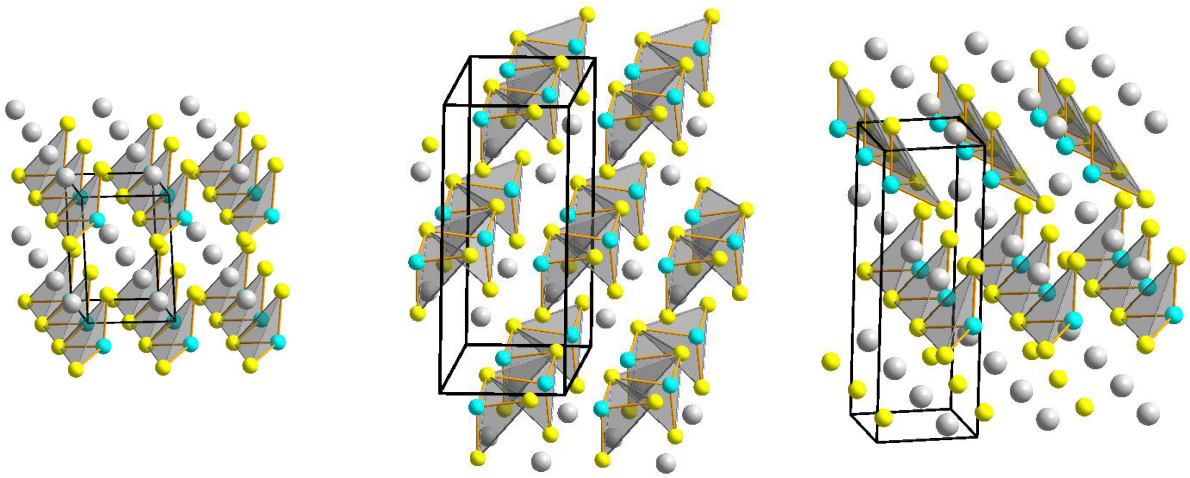

(a) (b) (c)

Figure 7

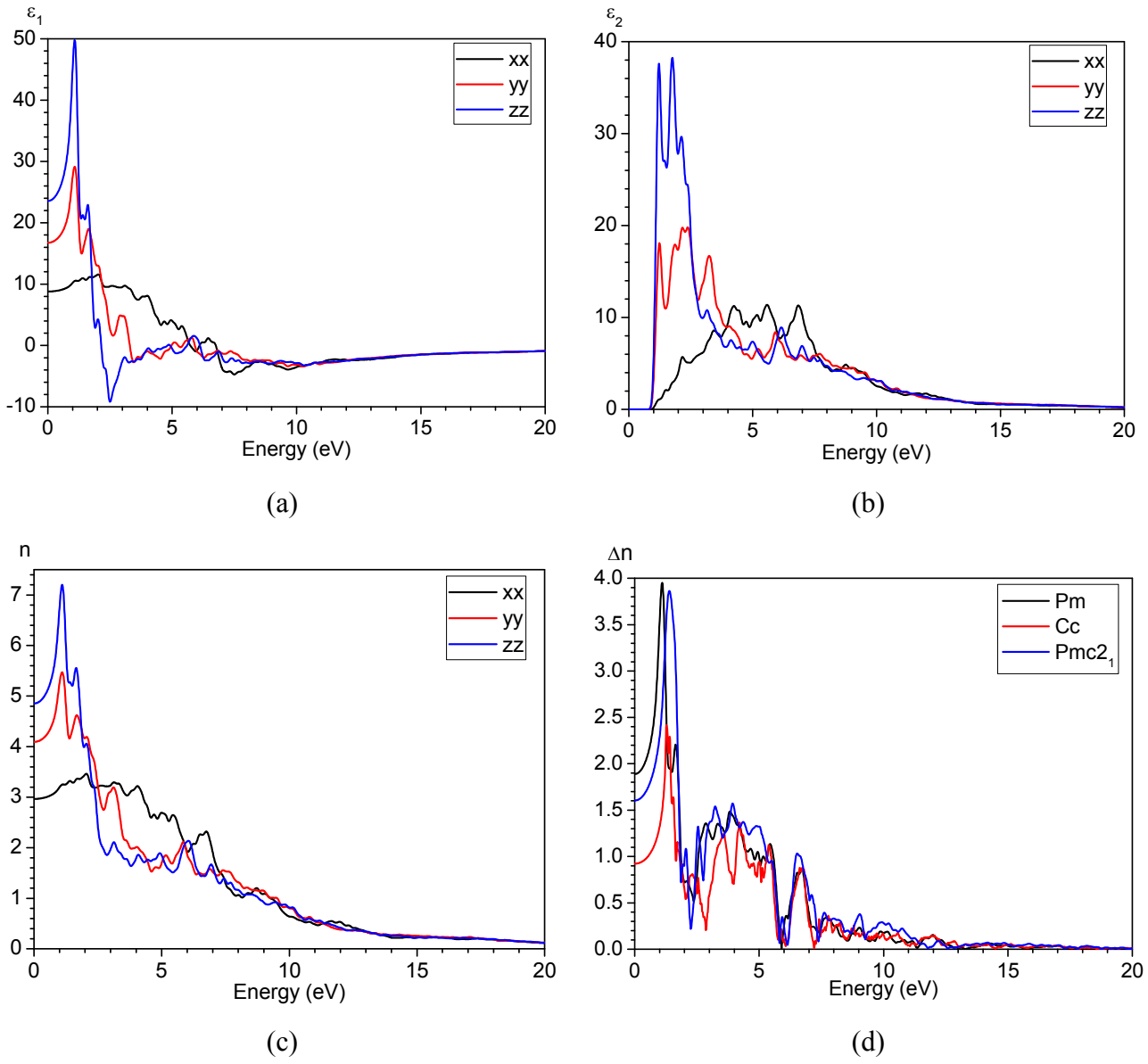

Figure 8

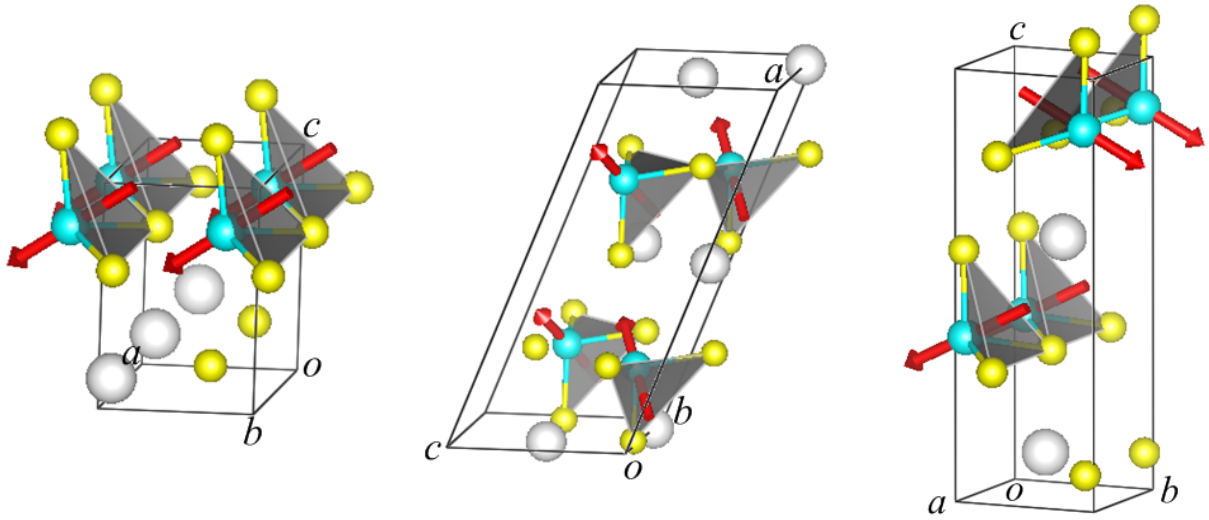

(a) (b) (c)

Table 1 The information of the best individual predicted by four test calculations using different methods for the $AgGaS_2$ crystals with different cell sizes [a]

Small cell that contains two Ag, two Ga, and four S atoms						
No.	Present GA method			USPEX method		
	Generation number	Source	Space group	Generation number	Source	Space group
1	3	Heredity	$I\bar{4}2d$	1	Random	$I\bar{4}2d$
2	1	Random	$I\bar{4}2d$	5	Heredity	$I\bar{4}2d$
3	1	Random	$I\bar{4}2d$	4	Heredity	$I\bar{4}2d$
4	1	Random	$I\bar{4}2d$	3	Mutation	$Pmc2_1$
Large cell that contains four Ag, four Ga, and eight S atoms						
No.	Present GA method			USPEX method		
	Generation number	Source	Space group	Generation number	Source	Space group
1	2	Heredity	$I\bar{4}2d$	8	Random	$I\bar{4}2d$
2	9	Heredity	$I\bar{4}2d$	7	Heredity	*Ima2*
3	6	Heredity	$I\bar{4}2d$	6	Mutation	$Pmc2_1$
4	4	Heredity	$I\bar{4}2d$	1	Random	*Ibam*

a. The population sizes and the maximum number of generations are 10 and 5, 30 and 10, for the small and large cells respectively, and the results of USPEX are obtained by the code of version 9.3.9.

Table 2 Space groups, some structural parameters, and the relative energies per formula of three stable $AgGaS_2$ crystals predicted by the GA approach

Structure	Figure 3a	Figure 3b	Figure 3c
Space group	$I\bar{4}2d$ (No. 122)	$Pna2_1$ (No. 33)	$Pmc2_1$ (No. 26)
Lattice parameters (Å)	a = b = 5.7889 (5.754)[a] c = 10.6573 (10.295)[a]	a = 6.7552, b = 8.0955 c = 6.5393	a = 3.7879, b = 7.1515 c = 6.5769
Fractional atomic positions	Ag: (0,0,0.5) Ga: (0,0,0) S: (0.78556,0.25,0.125)	Ag: (0.08799,0.62036,0.48337) Ga: (0.93246,0.87434,0.98766) S: (0.60294,0.85982,0.09331) S: (0.44011,0.61245,0.63152)	Ag: (0.5,0.83798,0.78760) Ga: (0,0.64891,0.30364) S: (0.5,0.81980,0.40265) S: (0,0.35672,0.44974)
Volume per formula ($Å^3$)	89.286	89.403	89.082
Ga-S bond length (Å)	2.326 (×4)	2.311, 2.323, 2.332, 2.334	2.328, 2.346 (×2), 2.300
Relative energy per formula (meV)	0	11.87	65.06

a. Experimental results.[45]

Table 3 The calculated static dielectric constants, refractive indices, birefringence, and SHG coefficient of $AgGaS_2$ crystallized in the $I\bar{4}2d$ space group

	ε(0)	n(0)	Δn(0)	SHG coefficient (pm/V)
This work	5.351($\varepsilon^{\perp}$), 5.154($\varepsilon^{//}$)	2.313($n^{\perp}$), 2.270($n^{//}$)	-0.043	17.47 (d_{36})
Other work:				
Ref. [47]	6.114($\varepsilon^{\perp}$), 5.940($\varepsilon^{//}$)	2.472($n^{\perp}$), 2.437($n^{//}$)	-0.035	
Ref. [48]	6.518($\varepsilon^{\perp}$), 6.677($\varepsilon^{//}$)	2.553($n^{\perp}$), 2.584($n^{//}$)	-0.031	14.10 (d_{36})
Experimental results:				
Ref. [49] (at 12.5 μm)		2.327($n^{\perp}$), 2.272($n^{//}$)	-0.055	
Ref. [50] (at 10.63 μm)		2.347($n^{\perp}$), 2.291($n^{//}$)	-0.056	
Ref. [51] (at 10.63 μm)			-0.047	18 ± 2.7 (d_{36})

Table 4 Space groups, some structural parameters, and the relative energies per formula of three stable $LiAsSe_2$ crystals predicted by the GA approach

Structure	Figure 6a	Figure 6b	Figure 6c
Space group	*Pm* (No. 6)	*Cc* (No. 9)	*Pmc2₁* (No. 26)
Lattice parameters (Å and degree)	a = 3.9928 b = 3.8228 c = 5.8532 β = 94.644	a = 12.5701 (12.287)[a] b = 5.5615 (5.542) c = 5.6179 (5.553) β = 112.754 (113.117)	a = 3.8199 b = 3.9873 c = 11.7254
Fractional atomic positions	Li: (0.64484,0,0.34045) As: (0.07365,0.5,0.90643) Se: (0.65545,0,0.81702) Se: (0.14702,0.5,0.31021)	Li: (0.0,0.73356,0.001) As: (0.71548,0.72131,0.17368) Se: (0.01240,0.76235,0.51870) Se: (0.75840,0.72478,0.77193)	Li: (0.5,0.56408,0.59856) As: (0,0.07295,0.38210) Se: (0.5,0.48051,0.33623) Se: (0,0.06143,0.58312)
Volume per formula ($Å^3$)	89.05	90.55	89.30
Distance between As and terminal Se (Å)	2.358	2.359	2.357
Distance between As and bridging Se (Å)	2.564	2.515, 2.554	2.565
Relative energy per formula (meV)	0	1.68	3.79

a. Experimental results are shown in parentheses. [5]

Table 5 Calculated band gap, static dielectric constants, refractive indices, birefringence, and the magnitudes of the SHG coefficient of $LiAsSe_2$ with different phases

	Pm	Cc	$Pmc2_1$
Band gap (eV)	0.346	0.671	0.333
$\varepsilon^{xx}(0)$	8.791	8.714	9.032
$\varepsilon^{yy}(0)$	16.753	15.007	15.551
$\varepsilon^{zz}(0)$	23.560	13.508	21.240
$n^{xx}(0)$	2.965	2.952	3.005
$n^{yy}(0)$	4.093	3.874	3.943
$n^{zz}(0)$	4.854	3.675	4.609
$\Delta n(0)$[a]	1.889	0.922	1.603
SHG coefficients (pm/V)	$d_{11}=48.52$, $d_{12}=d_{26}=45.43$ $d_{13}=d_{35}=260.48$ $d_{16}=d_{21}=61.23$ $d_{22}=535.41$ $d_{23}=d_{34}=1379.57$	$d_{11}=32.17$, $d_{12}=d_{26}=21.47$ $d_{13}=d_{35}=58.85$ $d_{15}=d_{31}=61.10$ $d_{24}=d_{32}=75.31$ $d_{33}=737.72$	$d_{11}=141.36$ $d_{12}=d_{26}=44.79$ $d_{13}=d_{35}=6.90$

a. In here, the birefringence is quantified as the maximum difference between three refractive indices exhibited by the material, namely $\Delta n(0)= n_{max}(0)-n_{min}(0)$.

Table 6 Calculated microscopic dipole moments μ (in Debye) of the $[AsSe_3]^{3-}$ groups in different $LiAsSe_2$ crystals [a]

	Pm	Cc		$Pmc2_1$	
μ_x	22.065	12.879	12.879	0	0.018
μ_y	0	-18.098	18.098	23.557	-23.536
μ_z	-14.178	15.689	15.689	-12.122	-12.115
μ_{total} (per Å^3)	0.295	0.224		0.136	

a. There are two $[AsSe_3]^{3-}$ groups in each unit cell for the Cc and $Pmc2_1$ structures.

References

1 C. Wang, T. Zhang and W. B. Lin, *Chem. Rev.*, 2012, **112**, 1084-1104.

2 K. M. Ok, E. O. Chi and P. S. Halasyamani, *Chem. Soc. Rev.*, 2006, **35**, 710-717.

3 I. Chung, J. I. Jang, C. D. Malliakas, J. B. Ketterson and M. G. Kanatzidis, *J. Am. Chem. Soc.*, 2010, **132**, 384-389.

4 I. Chung, J. H. Song, J. I. Jang, A. J. Freeman, J. B. Ketterson and M. G. Kanatzidis, *J. Am. Chem. Soc.*, 2009, **131**, 2647-2656.

5 T. K. Bera, J. I. Jang, J. H. Song, C. D. Malliakas, A. J. Freeman, J. B. Ketterson and M. G. Kanatzidis, *J. Am. Chem. Soc.*, 2010, **132**, 3484-3495.

6 T. K. Bera, J. H. Song, A. J. Freeman, J. I. Jang, J. B. Ketterson and M. G. Kanatzidis, *Angew. Chem. Int. Ed.*, 2008, **47**, 7828-7832.

7 S. Banerjee, C. D. Malliakas, J. I. Jang, J. B. Ketterson and M. G. Kanatzidis, *J. Am. Chem. Soc.*, 2008, **130**, 12270-12272.

8 S. Banerjee, J. M. Szarko, B. D. Yuhas, C. D. Malliakas, L. X. Chen and M. G. Kanatzidis, *J. Am. Chem. Soc.*, 2010, **132**, 5348-5350.

9 C. D. Morris, I. Chung, S. Park, C. M. Harrison, D. J. Clark, J. I. Jang and M. G. Kanatzidis, *J. Am. Chem. Soc.*, 2012, **134**, 20733-20744.

10 M. C. Chen, L. H. Li, Y. B. Chen and L. Chen, *J. Am. Chem. Soc.*, 2011, **133**, 4617-4624.

11 M. J. Zhang, B. X. Li, B. W. Liu, Y. H. Fan, X. G. Li, H. Y. Zeng and G. C. Guo, *Dalton Trans.*, 2013, **42**, 14223-14229.

12 Q. Wu, X. Meng, C. Zhong, X. Chen and J. Qin, *J. Am. Chem. Soc.*, 2014, **136**, 5683-5686.

13 G. Zhang, Y. Li, K. Jiang, H. Zeng, T. Liu, X. Chen, J. Qin, Z. Lin, P. Fu, Y. Wu and C. Chen, *J. Am. Chem. Soc.*, 2012, **134**, 14818-14822.

14 Y. Huang, X. Meng, L. Kang, Y. Li, C. Zhong, Z. Lin, X. Chen and J. Qin, *CrystEngComm*, 2013, **15**, 4196-4200.

15 Y. Dang, X. Meng, K. Jiang, C. Zhong, X. Chen and J. Qin, *Dalton Trans.*, 2013, **42**, 9893-9897.

16 H. W. Huang, J. Y. Yao, Z. S. Lin, X. Y. Wang, R. He, W. J. Yao, N. X. Zhai and C. T. Chen, *Angew. Chem. Int. Ed.*, 2011, **50**, 9141-9144.

17 H. W. Huang, L. J. Liu, S. F. Jin, W. J. Yao, Y. H. Zhang and C. T. Chen, *J. Am. Chem. Soc.*, 2013, **135**, 18319-18322.

18 H. P. Wu, H. W. Yu, Z. H. Yang, X. L. Hou, X. Su, S. L. Pan, K. R. Poeppelmeier and J. M. Rondinelli, *J. Am. Chem. Soc.*, 2013, **135**, 4215-4218.

19 G. H. Zou, L. Y. Zhang and N. Ye, *CrystEngComm*, 2013, **15**, 2422-2427.

20 M. Zhang, S. L. Pan, X. Y. Fan, Z. X. Zhou, K. R. Poeppelmeier and Y. Yang, *CrystEngComm*, 2011, **13**, 2899-2903.

21 I. Chung and M. G. Kanatzidis, *Chem. Mater.*, 2014, **26**, 849-869.

22 K. M. Ok, P. S. Halasyamani, D. Casanova, M. Llunell, P. Alemany and S. Alvarez, *Chem. Mater.*, 2006, **18**, 3176-3183.

23 W. G. Zhang and P. S. Halasyamani, *CrystEngComm*, 2012, **14**, 6839-6842.

24 Y. Yu, L. Y. Li, Z. B. Lin and G. F. Wang, *CrystEngComm*, 2013, **15**, 5245-5249.

25 W. L. Zhang, J. F. Sun, X. Q. Wang, G. Q. Shen and D. Z. Shen, *CrystEngComm*, 2012, **14**, 3490-3494.

26 N. Masó, D. I. Woodward, P. A. Thomas, A. Várezc and A. R. Westa, *J. Mater. Chem.*, 2011, **21**, 2715-2722.

27 W. G. Zhang, F. Li, S. H. Kim and P. S. Halasyamani, *Cryst. Growth Des.*, 2010, **10**, 4091-4095.

28 S. D. Nguyen, J. Yeon, S. H. Kim and P. S. Halasyamani, *J. Am. Chem. Soc.*, 2011, **133**, 12422-12425.

29 X. Xu, C. Hu, B. Li, B. Yang and J. Mao, *Chem. Mater.*, 2014, **26**, 3219-3230.

30 M. C. Chen, L. M. Wu, H. Lin, L. J. Zhou and L. Chen, *J. Am. Chem. Soc.*, 2012, **134**, 6058-6060.

31 S. L. Nguyen, J. I. Jang, J. B. Ketterson and M. G. Kanatzidis, *Inorg. Chem.*, 2010, **49**, 9098-9100.

32 A. R. Oganov, *Modern methods of crystal structure prediction*, John Wiley & Sons, 2011.

33 C. W. Glass, A. R. Oganov and N. Hansen, *Comput. Phys. Commun.*, 2006, **175**, 713-720.

34 A. R. Oganov, A. O. Lyakhov and M. Valle, *Acc. Chem. Res.*, 2011, **44**, 227-237.

35 G. Kresse and J. Hafner, *Phys. Rev. B*, 1993, **47**, 558-561.

36 G. Kresse and J. Furthmüller, *Phys. Rev. B*, 1996, **54**, 11169-11186.

37 G. Kresse and J. Furthmüller, *Comput. Mater. Sci.*, 1996, **6**, 15-50.

38 A. Togo, Spglib, http://spglib.sourceforge.net/.
39 J. L. Hughes and J. Sipe, *Phys. Rev. B*, 1996, **53**, 10751-10763.
40 C. Aversa and J. Sipe, *Phys. Rev. B*, 1995, **52**, 14636-14645.
41 S. N. Rashkeev, W. R. Lambrecht and B. Segall, *Phys. Rev. B*, 1998, **57**, 3905-3919.
42 D. Kleinman, *Phys. Rev.*, 1962, **126**, 1977-1979.
43 R. Liu, Y. F. Zhang and M. Q. Wang, The 11th International Symposium on Distributed Computing and Applications to Business, Engineering and Science, Guilin, China, 2012, 77-80.
44 Z. H. Levine and D. C. Allan, *Phys. Rev. Lett.*, 1991, **66**, 41-44.
45 G. Brandt, A. Räuber and J. Schneider, *Solid State Commun.*, 1973, **12**, 481-483.
46 J. L. Shay and J. H. Wernick, *Ternary chalcopyrite semiconductors: growth, electronic properties, and applications*, Pergamon Press Oxford, 1975.
47 S. Laksari, A. Chahed, N. Abbouni, O. Benhelal and B. Abbar, *Comput. Mater. Sci.*, 2006, **38**, 223-230.
48 L. Bai, Z. S. Lin, Z. Z. Wang, C. T. Chen and M. H. Lee, *J. Chem. Phys.*, 2004, **120**, 8772-8778.
49 G. Boyd, H. Kasper and J. McFee, *IEEE J. Quantum Electron.*, 1971, **7**, 563-573.
50 K. Kato and H. Shirahata, *Jpn. J. Appl. Phys.*, 1996, **35**, 4645-4648.
51 M. J. Weber, *Handbook of optical materials*, CRC press, 2002.
52 Z. J. Ma, K. C. Wu, R. J. Sa, Q. H. Li and Y. F. Zhang, *J. Alloys Compd.*, 2013, **568**, 16-20.
53 J. H. Song, A. J. Freeman, T. K. Bera, I. Chung and M. G. Kanatzidis, *Phys. Rev. B*, 2009, **79**, 245203.
54 Y. Porter, K. M. Ok, N. S. P. Bhuvanesh and P. S. Halasyamani, *Chem. Mater.*, 2001, **13**, 1910-1915.
55 I. D. Brown, *The Chemical Bond in Inorganic Chemistry: The Bond Valence Model*, Oxford University Press, 2002.